NJC

ROYAL SOCIETY OF CHEMISTRY

PAPER

View Article Online
View Journal | View Issue

Cite this: *New J. Chem.*, 2024, **48**, 10026

Computational exploration of panchromatic dye-sensitized solar cells with broad visible to near-infrared absorption: a density functional theory study†

Giuseppe Consiglio, *[a] Adam Gorczyński, [b] Guido Spoto,[c] Salvatore Petralia [d] and Giuseppe Forte *[d]

Density functional theory (DFT) calculations were carried out to investigate the absorption spectra and photoelectric properties of new metal-free dyes integrating an acene group positioned proximal to the donor moiety, exemplified by the 2-amino pyrrole. A linear carbon chain (LCC) with varying lengths serves as the link between the donor group and two distinct electron-attracting groups: cyanoacrylate and a derivative of pyridinium salt. Molecular orbital analysis reveals strategically positioned energy levels for efficient electron recovery, ensuring favorable thermodynamics for injection. UV-VIS absorption properties underscore superior outcomes for dyes with longer π–spacers, particularly those with pentacene showcase a panchromatic effect extending beyond 920 nm. Furthermore, the study explores the electron transfer process at the dye–semiconductor interface, emphasizing stable adsorption modes and favorable interactions. Photovoltaic property estimations, considering electron injection and recombination rates, indicate that dyes with pyridinium salt as the withdrawing group, specifically, **P-Pen-4-A2** and **P-Ant-4-A2**, exhibit excellent values for both open-circuit voltage (V_{oc}) and short-circuit photocurrent density (J_{sc}), thus demonstrating superior photovoltaic outcomes. The investigation of *J*–*V* curves predicts outstanding photoelectric conversion efficiency values of 29.72% and 27.90% for these dyes. Moreover, derivatives incorporating cyanoacrylate yields commendable PCE values of 20.30% and 25.01% for **P-Ant-4-A2** and **P-Pen-4-A2**. Classical molecular dynamics simulations (MD) demonstrate that, over the course of 200 ns simulation time, the dyes maintain a vertical adsorption configuration. These results underscore the potential of the designed dyes for both standalone and co-sensitizing applications, presenting a promising avenue for the development of efficient and panchromatic DSSCs.

Received 27th February 2024,
Accepted 2nd May 2024

DOI: 10.1039/d4nj00924j

rsc.li/njc

1. Introduction

In the pursuit of sustainable energy solutions, solar cells have emerged as a pivotal technology, offering a clean and renewable source of electricity. Among the various types of solar cells, dye-sensitized solar cells (DSSCs), have garnered significant attention due to their cost-effectiveness, ease of fabrication, and versatility in design.[1] Grätzel and O'Regan's groundbreaking work in 1991, introducing the concept of DSSCs, marked a paradigm shift in the field of photovoltaics.[2] Since then, researchers have continuously strived to enhance the performance of DSSCs through various innovations, including the choice of photoactive materials and optimization of device architecture. The integration of dyes as light-harvesting components plays a crucial role in determining the efficiency of DSSCs. In recent years, the focus has shifted towards enhancing the spectral response of these cells by employing dyes with broad absorption profiles, extending from the visible to the near-infrared (NIR) region.[3] This research endeavors to delve into the realm of panchromatic DSSCs, where the dye molecules exhibit absorption characteristics spanning a wide range of wavelengths, from visible to NIR, which represents *ca.* 45% of the solar irradiance until 1700 nm.[4] The selection of an appropriate dye molecule plays a crucial role in determining the absorption characteristics of DSSCs.[5] The implications of achieving panchromatic absorption are profound, not only enhancing the overall efficiency of solar energy conversion,

[a] *Department of Chemical Science, University of Catania, Via S. Sofia 64, 95125, Italy. E-mail: giuseppe.consiglio@unict.it*
[b] *Faculty of Chemistry, Adam Mickiewicz University, Uniwersytetu Poznańskiego 8, 61-614 Poznań, Poland*
[c] *InfoBiotech S.r.l, Via del Bersagliere 45, 90143 Palermo, Italy*
[d] *Department of Drug Science and Health, University of Catania, Via S. Sofia 64, 95125, Italy. E-mail: gforte@unict.it*

† Electronic supplementary information (ESI) available. See DOI: https://doi.org/10.1039/d4nj00924j

but also expanding the potential applications of these cells. The capability to capture sunlight across a wider spectrum makes panchromatic DSSCs particularly appealing for regions with variable weather conditions, low light levels, or indoor environments where traditional solar cells may falter.[6] Traditional dyes, such as ruthenium-based complexes, have demonstrated success in extending absorption capability into the NIR region.[7] Swetha *et al.* have designed and synthesized Ru-sensitizers that significantly enhance the absorptivity across the visible to NIR region, feature that is likely attributed to the pyrene conjugate on the terpyridine core.[8] In recent investigations, panchromatic DSSCs were developed incorporating a photoelectrode composed of bilayered TiO_2 thin films coated with N719, N749 and C106 dyes. A power conversion efficiency (PCE) of approximately 8% was achieved using a configuration in which the TiO_2 bottom layer was coated with C106 dye and the TiO_2 top layer with N719 dye.[9,10] Moreover, a novel panchromatic ruthenium polypyridyl complex was synthesized by substituting dicarboxylate–bipyridine ligands with their bipyrimidine counterparts, resulting in panchromatic Ru(II) complexes with absorption extending into the near IR region.[11] A category of Ru-derivative dyes was designed and utilized as co-sensitizers for N719 DSSC to address the insufficient light absorption in the visible region from 400 to 500 nm of N719 dye. Co-sensitization demonstrated a 19% improvement in power conversion energy compared to those employing N719 dyes alone.[12] The functionalization of terpyridine-coordinated ruthenium complex with 4-methylthiazole not only enhanced the lighting-harvesting capability of the dye molecule, but also increased the dye-loading in TiO_2 photoanode while reducing charge recombination in the cells. This resulted in a panchromatic response extending up to 900 nm and a PCE of 9.0%.[13] Sharmoukh *et al.* conducted research on *cis*-[Ru(bipyridine)$_2$ (phosphonic acid)$_2$]X$_2$ (X = Cl, SCN and CN) observing an increase in PCE in the following order –SCN > –CN > –Cl, with resulting PCE values of 1.91, 2.38 and 2.9%, respectively.[14] The research team also examined the impact of withdrawing groups on the fluorescence output of ruthenium-based complexes. They discovered that complexes with more withdrawing groups exhibited stronger emission peaks and shorter lifetimes, suggesting increased photoactivity. Among these groups, the ring nitrogen had the most significant impact on enhancing the emission spectra.[15] Another prominent class of dyes that has garnered attention in recent years includes derivatives of porphyrin.[16–22] These compounds exhibit distinctive optical properties and can be tailored to absorb light across a broad spectral range.[5] Di Carlo *et al.* investigated the photovoltaic applications of β-substituted dithienylethylene Zn(II) porphyrins in dye-sensitized solar cells.[23] The panchromatic effect, resulting from the elongation of π-delocalized system through a bridge between the dithienylethylene unit and the porphyrinic ring, was examined through electrochemical, computational and photoelectrochemical studies. These porphyrins demonstrate a panchromatic effect with broadened electronic absorption spectra due to the π-conjugated substituents at the β-pyrrolic position. The highest PCE achieved was 5.2% with a short-circuit photocurrent density (J_{sc}) value of 12.4 mA cm^{-2}. Xie and coworkers developed concerted companion dyes (CCD) by directly linking two subdye units with complementary absorption characteristics, leading to panchromatic absorption and excellent photovoltaic performance due to the intramolecular co-sensitization effect.[24–26] More recently, the same research group introduced a new dye that achieved a PCE of 12.2% without utilizing chenodeoxycholic acid as a coadsorbent to prevent aggregation. These results highlight the doubly concerted effects, wherein the complementary absorption of the porphyrin and organic units contributes to panchromatic spectra.[27] The emergence of organic metal-free dyes has opened up possibilities to create novel panchromatic DSSCs with absorption extending into the NIR region.[5] A dye featuring panchromatic characteristics was synthesized through a synergistic combination of boron dibenzopyrromethene-conjugated phenothiazine, utilizing cyanoacrylic acid as the anchoring group. Results demonstrated an intense absorption band at about 640 nm, an excellent J_{sc} value and a PCE of 7.69%.[28] *cis*-Configured and π-extended unsymmetrical squaraine dyes were systematically designed and synthesized to enhance the light-harvesting efficiency across both the visible and NIR regions.[29] The *cis*-squaraine played a pivotal role in extending conjugation into the NIR region, achieving a panchromatic sensitizer. To modulate dye assembly on TiO_2 both out of plane and in-plane groups were introduced. The best-performing configuration exhibited solar-to-electric conversion with an onset of 850 nm, yielding a performance of 7.0%.[29] Co-sensitization emerged as an effective strategy to achieve panchromatic light-harvesting and to enhance dye-sensitized solar cell performance. Three organic dyes, containing butyloxyl chain induced dye, boron dipyrromethene dye and a squaraine-based dye, were co-sensitized obtaining panchromatic absorption in the 300–820 nm range, yielding a J_{sc} of 15.57 mA cm^{-2} and an optimal efficiency of 7.48%.[30] Following a similar strategy, Golshan *et al.* assessed extracted natural dyes as mono and co-sensitizers in DSSCs. The UV-vis absorption spectra indicated superior activity, showcasing a high molar extinction coefficient and cumulative absorption properties that overlapped with the spectral domain where the original sensitizers lacked light-harvesting.[31] Furthermore, the co-sensitization of dyes featuring an indoline donor group and the unsymmetrical squaraine yielded a solar cell efficiency of 5.20%, with UV-vis absorption bands between 337–385 nm, 477–514 nm and a third absorption band in the region between 629–758 nm, observed for the first time in a D–π–A type dye architecture.[32,33] In recent computational studies, we delved into the optoelectronic characteristics and potential performance of a novel D–π–A structured dye class in DSSC applications. The π-bridge consisted of a linear carbon chain, with cyanoacrylic acid acting as the acceptor (A1) and 2-amine pyrrole as the donor group (D).[34,35] The best calculated performance reached a PCE of 21.29%. Subsequently, we examined the charge transfer efficiency of the 2-amine pyrrole donor group, along with various electron-attracting groups. This investigation highlighted that pairing 2-amine pyrrole with a unique electron-attracting group, a derivative of a pyrimidin–pyridinium salt not conventionally used in photovoltaic applications, henceforth named A2, resulted in superior

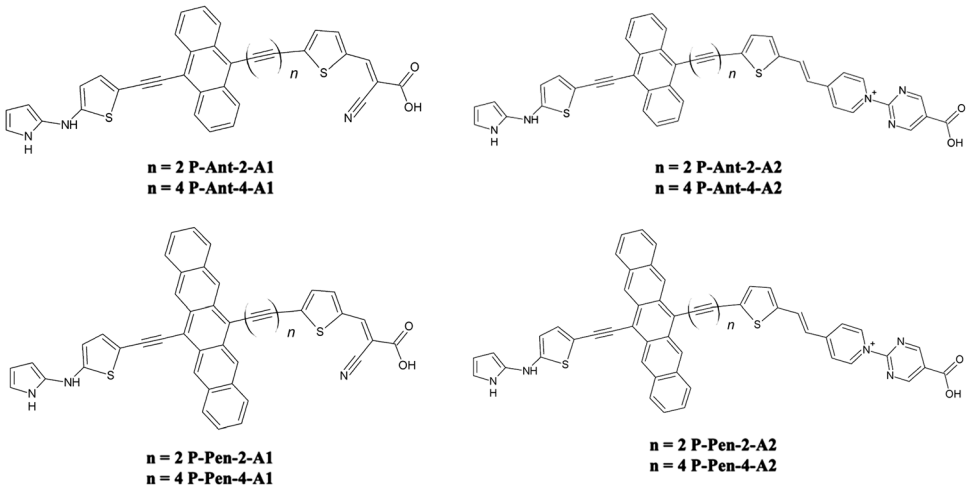

Scheme 1 Molecular structure of the designed dyes. In details **P-Ant-2-A1** is (*E*)-3-(5-((10-((5-((1*H*-pyrrol-2-yl)amino)thiophen-2yl)ethynyl)anthracene-9-yl)buta-1,3-diyn-1-yl)thiophen-2-yl)-2-cyanoacrilic acid; **P-Ant-4-A1** is (*E*)-3-(5-((10-((5-((1*H*-pyrrol-2-yl)amino)thiophen-2yl)ethynyl)anthracene-9-yl)octa-1,3,5,7-tetrayn-1-yl)thiophen-2-yl)-2-cyanoacrilic acid; **P-Ant-2-A2** is (*E*)-4-(2-(5-((10-((5-((1*H*-pyrrol-2-yl)amino)thiophen-2yl)ethynyl)anthracen-9-yl)buta-1,3-diyn-1-yl)thiophen-2-yl))-1-(5-carboxypyrimidin-2yl)pyridin-1-ium; **P-Ant-4-A2** is (*E*)-4-(2-(5-((10-((5-((1*H*-pyrrol-2-yl)amino)thiophen-2yl)ethynyl)-anthracen-9-yl)octa-1,3,5,7-tetrayn-1-yl)thiophen-2-yl)vinyl)-1-(5-carboxypyrimidin-2yl)pyridin-1-ium; **P-Pen-2-A1** is (*E*)-(5-((13-((5-((1*H*-pyrrol-2-yl) amino)thiophen-2-yl)ethynyl)pentacene-6-yl)buta-1,3-diyn-1-yl)thiophen-2-yl)-2-cyanoacrylic acid; **P-Pen-4-A1** is (*E*)-(5-((13-((5-((1*H*-pyrrol-2-yl) amino)thiophen-2-yl)ethynyl)pentacen-6-yl)octa-1,3,5,7-tetrayn-1-yl)thiophen-2-yl)-cyanoacrylic acid; **P-Pen-2-A2** is (*E*)-4-(2-(5-((13-((5-((1*H*-pyrrol-2-yl)amino)thiophen-2-yl)ethynyl)pentacen-6-yl)buta-1,3,diyn-1-yl)thiophen-2-yl)vinyl-1-(5-carboxypyrimidin-2-yl)pyridinium); **P-Pen-4-A2** is (*E*)-4-(2-(5-((13-((5-((1*H*-pyrrol-2-yl)amino)thiophen-2-yl)ethynyl)pentacen-6-yl)octa-1,3,5,7-tetrayn-1-yl)thiophen-2-yl)vinyl-1-(5-carboxypyrimidin-2-yl)pyridinium).

characteristics compared to commonly used donor and acceptor groups in photovoltaics, such as phenothiazine and cyanoacrylic acid.[36] However, the UV-vis spectra of the previously modeled dyes reveal a limitation arising from maximum wavelength absorption, occurring at around 550 nm. This results in the loss of a significant portion of available solar energy. In an effort to broaden the absorption range and design panchromatic-active sensitizers with strong absorption in the far-red and near-infrared regions, this study introduces acene groups into the donor moiety of dyes featuring D as donor group. The remaining part of the dyes comprises the π-linker, represented by a linear carbon chain (LCC) of varying lengths (C_4, C_8) along with two distinct electron-acceptor groups, the cyanoacrylic group, A1, and the pyrimidin–pyridinium salt derivative, A2, see Scheme 1. The inclusion of linear fused benzene rings was inspired by previous research demonstrating that introducing different acenes into the porphyrin core results in a broadening and red-shifting of absorption with an increase in acene size.[37] Moreover, acenes confer structural rigidity to the dye skeleton. This characteristic is expected to enhance the photovoltaic performance of the dyes, as suggested by studies conducted by Li *et al.*, which examined the impact of spacer rigidification and observed improved performance performance.[38,39] Specifically, anthracene and pentacene groups were linked, on one side, to the donor moiety, through a triple bond to alleviate steric congestion between the acene group and the neighboring thiophene ring, and, on the other side, to the π-linker. It is noteworthy that LCCs demonstrate electrical conduction and possess unique optoelectronic properties owing to their extensive π-conjugated system.[40–45] Thiophene rings were incorporated based on literature suggesting the efficiency of dithiophene derivatives in the π-linker.[46–49] Additionally, an ethylenic bridge was introduced to connect the thiophene ring with the acceptor group, enhancing the planarity of the structure. Classical MD simulations were performed to investigate the potential for the dyes to undergo surface collapse. In summary, through harnessing progress in molecular design, our objective is to extend the absorption spectrum towards the NIR by developing panchromatic dyes, with a potential use as standalone sensitizers or co-sensitizers, aiming to push the limits of solar cell efficiency and enhance the practical uses of DSSCs. The ultimate goal is to actively contribute to the continuous endeavors in achieving sustainable and efficient technologies for converting solar energy.

2. Methods

The Gaussian 16 program package[50] was utilized for conducting molecular simulations on the examined dyes. The geometries of all compounds underwent fully optimization through the B3LYP functional with the 6-311+G(2d,p) basis set. To calculate UV-VIS spectra, the TD-DFT approach with the same basis set was employed, focusing on the lowest 10 singlet–singlet transitions. The CAM-B3LYP functional was chosen because, as demonstrated in previous studies, it consistently produced UV-VIS spectra closely aligned with experimental data for compounds sharing a similar structural framework.[51,52] However, for comparison, WBX97D and M062X functionals were employed. To account for solvation effects, the solvated method based on density (SMD) was adopted. When comparing this approach with the conductor-like polarizable continuum model (CPCM) and IEFPCM methods, minimal variations were observed in both UV-vis absorption values and absorption intensities.[34–36] Such consistency has led to the persistent

application of this model in investigations. It's important to mention that the molecules studied in this paper are currently not available experimentally, consequently, there are no experimental data for comparison. The adsorption of dyes showcasing superior optical performance on the TiO_2 semiconductor was simulated using a vacuum slab derived from a 2 × 2 × 4 TiO_2 anatase (101) supercell containing a total of 768 atoms ($Ti_{256}O_{512}$). The dyes were arranged perpendicular to the surface, and a 1 nm vacuum region was included above the dye to minimize interactions with the periodic image. Consequently, the simulation cell had dimension of 3.87 × 3.02 × 5.75 nm^3, see Fig. S1 (ESI†). The structures underwent optimization using the general gradient approximation, employing the Perdew–Burke–Erzerhof functional to account for electron exchange and correlation effects. Broyden–Fletcher–Goldfarb–Shanno (BFGS) minimization algorithm was utilized for geometry optimization, and the dipole correction was implemented with the self-consistent option. Convergence criteria were established with an energy cutoff of 40 Ry and a maximum force of 10^{-4} Ry $Bohr^{-1}$ for each atom. The dyes were linked to the TiO_2 surface by bonding the two oxygen atoms of the dye's acid group to two titanium atoms. This choice is substantiated by prior studies demonstrating the bidentate mode as the most stable binding geometry.[53–55] Computations for the dyes@TiO_2 systems were conducted using the Quantum Espresso simulation package.[56,57] Classical MD simulations were ultimately carried out applying the OPLS all-atom force field parametrization *via* the Gromacs software package,[58,59] starting from the geometries obtained post-optimization with Quantum Espresso. A simulation time of 200 ns was established, employing periodic boundary conditions and adopting the NVT ensemble at a temperature of 298 K controlled with the Berendsen thermostat with a decay constant set to 0.1 ps. The Ewald summation method was chosen to address long-range electrostatic interactions, considering a cutoff distance of 2.0 nm and a time step of 1 fs was selected to integrate the equation of motion.[60–62]

2.1 Theoretical background

The photoelectric conversion efficiency, η, for a solar cell device can determined through the formula:[63]

$$\eta = \frac{J_{sc} \cdot V_{oc}}{P_{in}} \cdot \mathrm{FF} \tag{1}$$

where P_{in} denotes the incident solar power on the cell and FF represents the fill factor. The short circuit current, J_{sc}, is derived from the following expression:[64]

$$J_{sc} = q\int \mathrm{LHE}(\lambda)\Phi_{inj}\eta_{reg}\eta_{coll}\vartheta_{ph.AM\,1.5G}(\lambda)\mathrm{d}\lambda \tag{2}$$

the integration occurs within the wavelength range of 280 to 920 nm. In this context q symbolizes the elementary charge of the electron, $\vartheta_{ph.AM\,1.5G}$ corresponds to the photon flux under AM 1.5G solar spectra irradiance, and Φ_{inj} stands for the electron injection efficiency, defined as:[65]

$$\Phi_{inj} = \frac{1}{\left(1 + \frac{\tau_{inj}}{\tau_{relax}}\right)} \tag{3}$$

here τ_{relax} is the relaxation lifetime of the dye's excited states and τ_{inj} represents the injection time. In eqn (2) η_{reg} is the dye regeneration efficiency set equal to 1, and η_{coll} denotes the electron collection efficiency expressed as:[66]

$$\eta_{coll} = \frac{1}{\left(1 + \frac{\tau_{trans}}{\tau_{rec}}\right)} \tag{4}$$

where τ_{trans} is the electron-transport time from the semiconductor's conduction band to the electrode and τ_{rec} denotes the recombination time the light harvesting efficiency, LHE, is related to the dye absorption region through the equation:[67]

$$\mathrm{LHE}(\lambda) = 1 - 10^{-\varepsilon(\lambda)\Gamma} \tag{5}$$

where $\varepsilon(\lambda)$ represents the molar absorption coefficient at a specific wavelength, while Γ is the surface loading of dye, calculated as the product of dye concentration c and TiO_2 film thickness b. A time of 10 ps is adopted for both τ_{relax} and τ_{trans}. The values of Φ_{inj} and η_{coll} depend on $\tau_{inj/rec}$, the reciprocal of $k_{inj/rec}$ which can be calculated, according to the Marcus theory, as:[68]

$$k_{inj/rec} = A\sqrt{\frac{\pi}{\hbar^2\lambda k_B T}}\exp(-\beta r)\exp\left(\frac{-\left(-\Delta G^0_{inj/rec} + \lambda\right)^2}{4\lambda k_B T}\right) \tag{6}$$

here $A = 2.5 \times 10^{-2}$, β is the attenuation factor, set to 0.5, r represents the electron transfer distance. The parameter λ corresponds to the sum of the hole and electron reorganization energy ($\lambda_h + \lambda_e$), it is assumed to be identical for injection and reorganization and is calculated as:[69]

$$\begin{aligned}\lambda_e &= \left(E_0^- - E_-\right) + \left(E_-^0 - E_0\right)\\ \lambda_h &= \left(E_0^+ - E_+\right) + \left(E_+^0 - E_0\right)\end{aligned} \tag{7}$$

In this contest, $E_0^{+/-}$ represent the energies of the cation and anion derived from the geometry of the optimized neutral molecule; $E_{+/-}$ refers to the energies of the cation and anion calculated based on the optimized cation and anion; $E^0_{+/-}$ are the energies of the neutral molecules calculated from the optimized cation and anion; E_0 corresponds to the energy of the neutral dye molecule in its ground state. The prediction of the open-circuit voltage (V_{oc}) can be achieved through the improved normal model (INM) method, which incorporates the effects of charge recombination and various parameters related to the device fabrication, including electrolyte concentration and film thickness. Following this methodology, V_{oc} can be determined by the following expression:[70]

$$V_{oc} = \frac{k_B T}{\beta' q}\ln\frac{\beta' q R_0 J_{sc}}{k_B T} \tag{8}$$

where k_B is the Boltzmann constant, T denotes the absolute temperature, β' represents the charge transfer coefficient for electron recombination (empirically set at 0.5), and R_0 is the recombination resistance, measured in Ohm cm^2, defined as:

$$R_O = \frac{\sqrt{\pi\lambda k_B T}}{q^2 \mathrm{d}\gamma k_{rec} M_{ox} N_S}\exp\left(\gamma\frac{E_{CBM} - E_{redox}}{k_B T} + \frac{\lambda}{4k_B T}\right) \tag{9}$$

in this equation d signifies the film thickness, an experimental

value of 10^{-3} cm was considered;[71] M_{ox} refers to the molarity of the electrolyte oxidized species, with I_3^- set to 0.05 in this instance; N_s represents the total number of surface states contributing to the recombination, set to 10^{-5}; the parameter γ is equal to 0.3 based on typical experimental data;[72,73] E_{CBM} is the TiO_2 conduction band minimum, while E_{redox} denotes the electrolyte redox potential.

3. Results and discussion

3.1 Frontiers molecular orbitals analysis and absorption spectra

DSSCs hold promise for efficient solar energy utilization, with the energy levels of the dye sensitizers playing a crucial role in their performance. One prerequisite is the appropriate energy level of the LUMO, which facilitates efficient electron injection into the TiO_2 conduction band (CB). Additionally, an optimal HOMO energy level is essential for efficient electron collection. In Fig. 1, the energy diagram of selected molecular orbitals (MOs) for the investigated dyes is presented. Notably, all compounds exhibit HOMO energy levels positioned below −4.8 eV, the redox potential of the electrolyte I^-/I_3^- relative to the vacuum level.[74] This positioning ensures efficient electron recovery. All LUMO levels are above the CB of TiO_2 (−4.0 eV)[75] with energy differences much greater than 0.2 eV, approximately the value above which an efficient electron injection is thermodynamically favorable.[76]

Understanding the absorption properties of dye sensitizers is crucial for optimizing their performance in DSSCs. Fig. 2 illustrates the UV-vis absorption spectra of the investigated molecules, revealing a distinct peak in the visible region with significant intensity corresponding to the HOMO → LUMO transition, indicative of intermolecular charge transfer (ICT), see Table 1 and Fig. 2. Additionally, a secondary UV absorption band attributed to π–π* transitions is observed. The spatial distribution of the frontier MOs, Fig. 3, reveals electron density moving through the π-linker from the dye-donor side, HOMO, to the acceptor end, LUMO, facilitating the ICT process. The overlapping HOMO and LUMO orbitals across the π-linker demonstrate excellent induction and electron-withdrawing properties for both donor and acceptor moieties, further enhancing the ICT process. The shortening of the LCC bridge induces a slight blue-shift and a substantial decrease in band intensity. Regarding the two investigated electron-attracting groups, dyes incorporating A2 exhibit a significant increase in absorption intensity and subtle redshifts in the absorption wavelength when compared to the cyanoacrylate

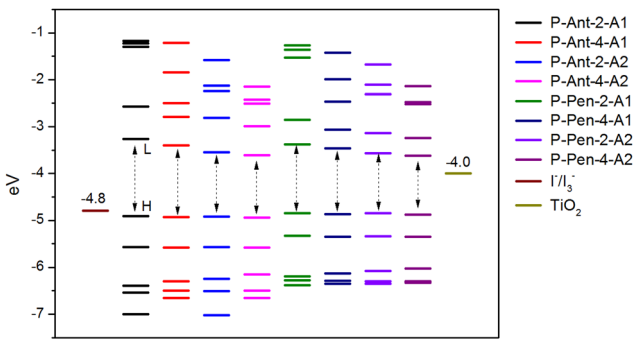

Fig. 1 Selected MOs energy levels for the designed dyes at B3LYP/6-311+G(2d,p)/SMD level together with TiO_2 CB and I^-/I_3^- redox potential (H = HOMO, L = LUMO).

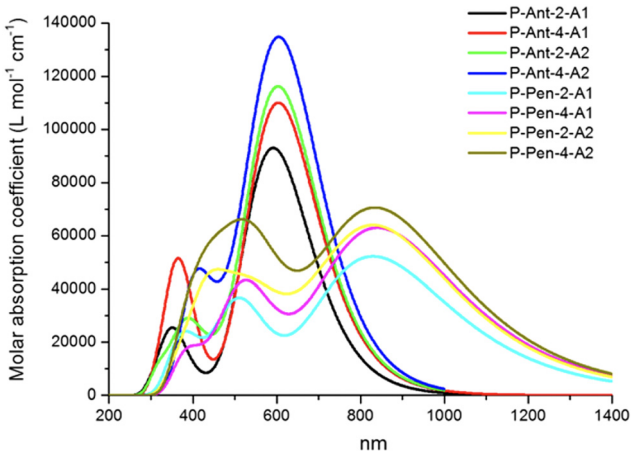

Fig. 2 Absorption spectra of dyes in acetonitrile at TD-CAM-B3LYP/6-311+G(2d,p)/SMD level. The spectra are Gaussian broaded with 0.35 eV (half width half maximum).

Table 1 Absorption wavelengths, oscillator strength, and main contributions ($f > 0.2$) to the transitions of dyes in acetonitrile at CAM-B3LYP/6-311+G(2d,p)/SMD level

Compound	λ (nm)	λ (eV)	f	μ (Debye)	Main contribution to the transition
P-Ant-2-A1	590.71	2.10	2.30	14.91	H → L (70%)
	356.04	3.48	0.50		H−2 → L (50%)
P-Ant-4-A1	604.21	2.05	2.71	15.88	H → L (61%)
	376.67	3.29	0.40		H−2 → L (39%)
	363.16	3.41	0.78		H−4 → L+2 (34%)
	325.03	3.81	0.27		H → L+4 (51%)
P-Ant-2-A2	604.80	2.05	2.84	37.62	H → L (60%)
	467.09	2.65	0.25		H → L+1 (44%)
	383.32	3.23	0.56		H−2 → L (30%)
P-Ant-4-A2	608.06	2.04	3.26	50.23	H → L (42%)
	481.41	2.58	0.37		H → L+2 (41%)
	407.59	3.04	1.02		H−2 → L (24%)
P-Pen-2-A1	831.49	1.49	1.29	19.60	H → L (90%)
	517.72	2.39	0.69		H → L+1 (72%)
	494.77	2.51	0.20		H−1 → L (72%)
	395.81	3.13	0.35		H−2 → L (73%)
	357.92	3.46	0.22		H → L+2 (77%)
P-Pen-4-A1	843.48	1.47	1.55	21.79	H → L (84%)
	534.99	2.32	0.78		H → L+1 (56%)
	504.69	2.46	0.27		H−1 → L (68%)
	380.48	3.26	0.22		H → L+3 (39%)
P-Pen-2-A2	838.46	1.48	1.55	34.44	H → L (65%)
	564.30	2.20	0.76		H → L+1 (55%)
	493.54	2.51	0.30		H−1 → L (49%)
	436.85	2.84	0.83		H−2 → L (72%)
P-Pen-4-A2	842.79	1.47	1.71	47.49	H → L (55%)
	554.83	2.23	1.15		H → L+1 (35%)
	503.40	2.46	0.29		H−1 → L (42%)
	448.42	2.76	0.75		H−2 → L (55%)
	422.70	2.93	0.25		H → L+2 (28%)
	382.31	3.24	0.46		H−2 → L+1 (24%)

group. Furthermore, these derivatives display a notably remarkable dipole moment, suggesting potential applications in nonlinear optics, as illustrated in Table 1. The absorption spectra clearly show that the introduction of pentacene results in a

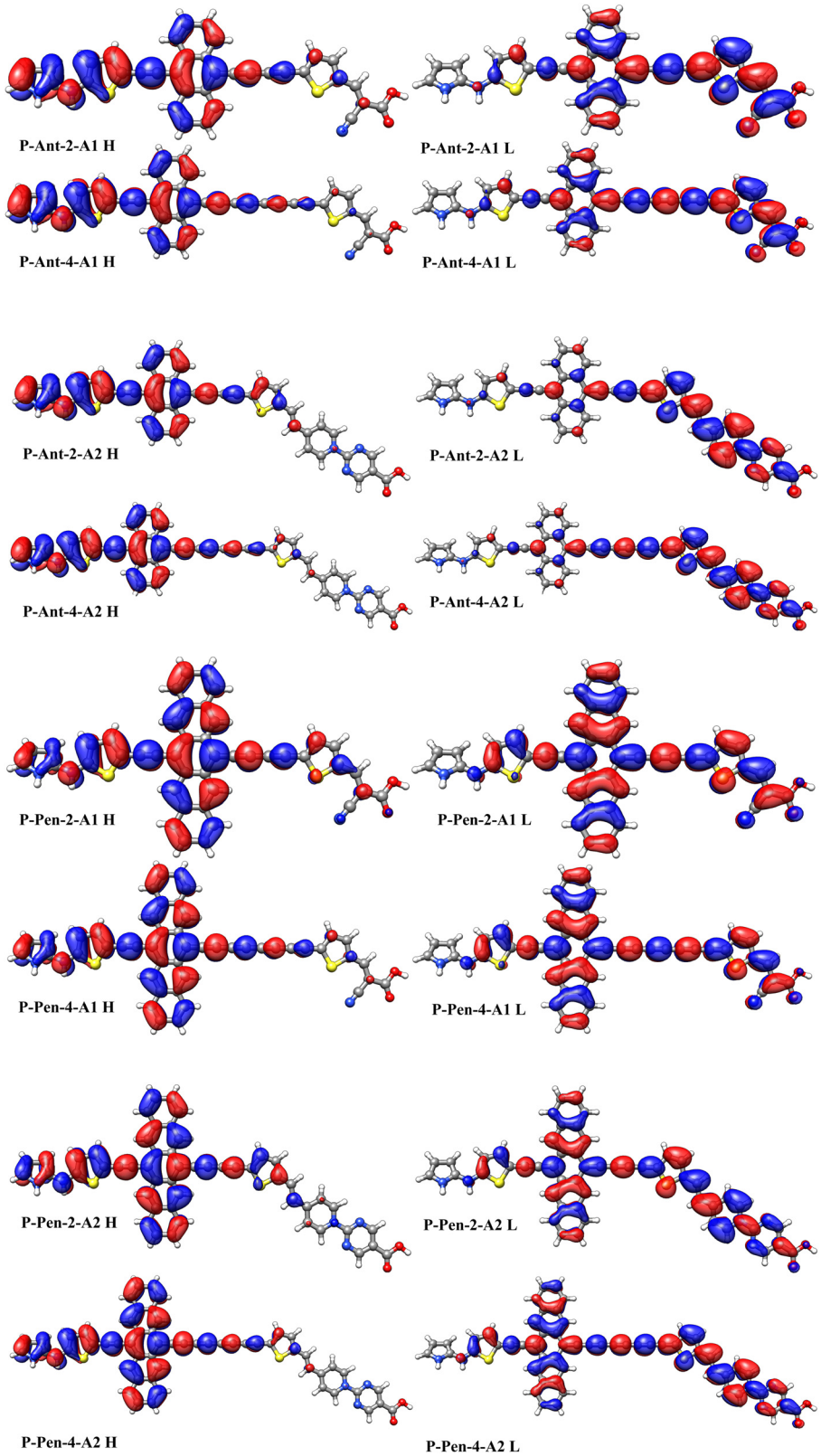

Fig. 3 Frontiers MOs of HOMO and LUMO of the dyes in acetonitrile at TD-CAM-B3LYP/6-311+G(2d,p)/SMD level.

marked redshift of the maximum absorption wavelength, extending beyond 800 nm. In contrast, anthracene exhibits a different behavior, showing maximum absorption at a shorter wavelength, around 600 nm, but with a highly pronounced intensity. The UV-vis spectra calculated using WBX97D and M062X functionals for the most efficient molecules containing anthracene and pentacene closely match the results obtained through the application of CAM-B3LYP, as shown in the ESI.†

To assess the impact on photovoltaic properties, it is essential to consider both absorption intensity and the optical absorption range. These combined data can be summarized by the light harvesting efficiency value, which helps in calculating the dye's efficiency and can be determined using the eqn (5). The LHE(λ) curves along with the AM 1.5G solar spectrum are reported in Fig. 4, showcasing findings for dyes featuring longer linear carbon chain, as they exhibit superior outcomes. Molecules bearing pentacene demonstrate the most remarkable LHE(λ) values, calculated across the spectrum from 280 to 920 nm. Nevertheless, dyes containing anthracene also exhibit excellent LHE values, especially within the range of 500–700 nm. Notably, the overlap of UV-vis absorptions, and, consequently, the overlap of LHE(λ) curves, results in a panchromatic effect that spans extensively from 350 to well beyond 920 nm. Optimal outcomes concerning this property are observed when employing the pyridine salt an electron-attracting group, with respect to cyanoacrylate.

3.2 TiO_2–dye adsorption

To explore the electron transfer process at the interface, attention was directed towards the electron transfer process occurring at the interface between dye and semiconductor, by closely examining the absorption complexes of dyes@TiO_2.

In particular, derivatives with an extended linear carbon chain bridge, LCC = 4, were considered as they exhibited superior values of LHE(λ) in comparison to those with a shorter LCC.

In all instances, we opted for bidentate bridging mode, which has been documented as the most stable adsorption mode. In this model, the sensitizer establishes binding with the semiconductor through two O–Ti bonds, whereas the protonated hydrogen atom is donated to the nearest double-coordinated surface oxygen atom. The calculated adsorption energies are determined as follows:

$$E_{ads} = E_{Dye@TiO_2} - (E_{TiO_2} + E_{Dye})$$

The corresponding values listed in Table 2, indicate highly favorable interactions between the dyes and the surface. Fig. 5 illustrates the partial density of states (PDOS) for the interfaces of dyes@TiO_2. It is evident that, subsequent to adsorption, the calculated LUMO energy levels of all sensitizers remain positioned above the conduction band minimum (CBM) of TiO_2, ensuring an efficient driving force for electron transfer to the semiconductor's CB, see Table 2. Additionally, the HOMO energy levels undergo a shift towards lower values upon adsorption, increasing the energy difference relative to the electrolyte redox potential. This adjustment ensures a favorable ground-state dye regeneration, leading to a significant improvement in the V_{oc} value and, consequently, enhancing the overall performance, as further discussed below. To validate this prediction, we proceeded to calculate the photoelectric conversion efficiency.

3.3 Estimation of photovoltaic properties

Up to this point we have obtained the absorbance of the sensitizer, moreover, it is evident from data reported in Table 2 that both electron injection and electron recombination are conducive to ensuring efficient electron transfer and ground-state dye recombination. The remaining task involves calculating the photoelectric conversion efficiency, η, of solar cell device, as defined by eqn (1). For this purpose, we calculated the reorganization energy λ, along with the electron injection rate, k_{inj}, and electron recombination, k_{rec}, rate, following the eqn (6). The computed values are presented in Table 3.

It is worth noting that dyes featuring A2 exhibit lower values of k_{rec}, indicating longer recombination times, which positively influences the V_{oc} values. Conversely, dyes containing cyanoacrylate demonstrate higher electron injection rate, k_{inj}. Based on these values and assuming a time of 10 ps for both τ_{relax} and τ_{trans}, it is inferred that the values of Φ_{inj} and η_{coll}, which are inversely related to $k_{inj/rec}$, are equal to 1. In light of this considerations, J_{sc} values can be easily obtained from the following equation:

$$J_{sc} = q\int_{280}^{920} \mathrm{LHE}(\lambda)\vartheta_{ph.AM\ 1.5G}(\lambda)\mathrm{d}\lambda$$

Among the investigated dyes, the predicted J_{sc} values follow the order **P-Pen-4-A2** > **P-Pen-4-A1** > **P-Ant-4-A2** > **P-Ant-4-A1**. These

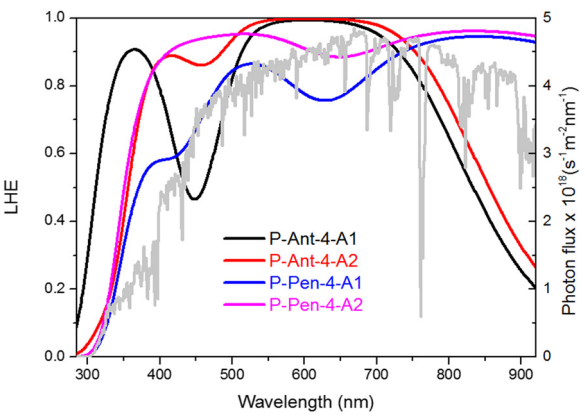

Fig. 4 LHE(λ) curves of selected dyes (Γ = 20 nmol cm^{-2} is taken in all cases). AM 1.5G solar spectrum is reported in grey.

Table 2 Adsorption energies, E_{ads}, energy levels and driving forces for the selected dyes@TiO_2 complexes (energies in eV)

Compound	E_{ads}	HOMO	LUMO	CBM	ΔG^0_{inject} [a]	ΔG^0_{rec} [b]
P-Ant-4-A1@TiO_2	0.77	−5.06	−3.11	−3.79	0.68	1.27
P-Ant-4-A2@TiO_2	0.73	−5.09	−3.15	−3.83	0.68	1.26
P-Pen-4-A1@TiO_2	0.75	−5.04	−3.12	−3.77	0.65	1.27
P-Pen-4-A2@TiO_2	0.70	−5.08	−3.18	−3.85	0.67	1.23

[a] $\Delta G^0_{inject} = E_{LUMO} - E_{CBM}$. [b] $\Delta G^0_{rec} = E_{CBM} - E_{HOMO}$.

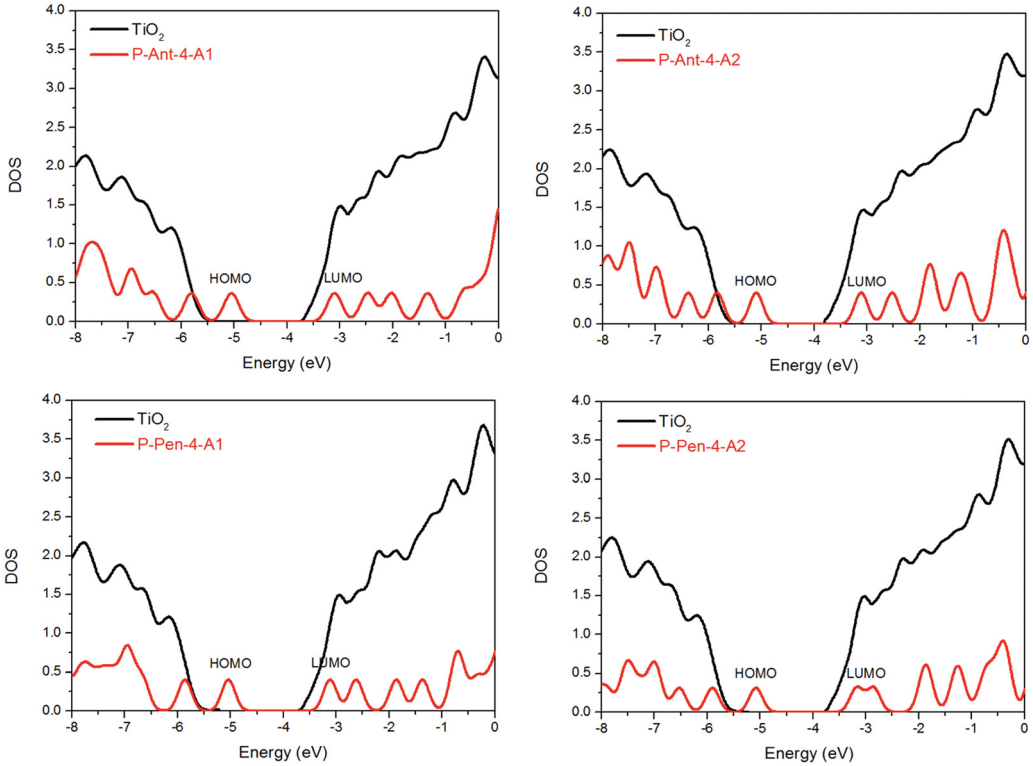

Fig. 5 Calculated PDOS for **P-Ant-4-A1**, **P-Ant-4-A2**, **P-Pen-4-A1** and **P-Pen-4-A2**.

results highlight the role played by the pentacene group in comparison with anthracene, and, secondarily, the enhanced performance attributed to the use of A2 as the electron attracting group. Another pivotal factor significantly affecting the overall cell efficiency is V_{oc}, defined as the difference between the electrolyte redox potential and the quasi-Fermi level of electrons within the semiconductor. The precise evaluation of this parameter is attainable through the utilization of the improved normal model (INM). During the injection process, there occurs an electron transfer from the LUMO of the dye to the semiconductor surface, with the distance from the anchoring group of the dye to the TiO_2 surface is denoted as r_{inj}. Conversely, in the recombination process, electron transfer takes place from the TiO_2 CB to the HOMO of the dye, and r_{rec} designates the distance between the semiconductor and the donor group of the dye. According to eqn (8) and (9), **P-Ant-4-A2** displays the slowest charge recombination rate, resulting in the highest predicted V_{oc} value, 1109 mV, followed by **P-Pen-4-A2** with a value of 1012 mV. On the other hand, both **P-Ant-4-A1** and **P-Pen-4-A1** exhibit a higher recombination rate constant ranging between one and two orders of magnitude, leading to diminished V_{oc} values, specifically, 937 mV is calculated for **P-Ant-4-A1** and 884 mV for **P-Pen-4-A1**. Employing the obtained J_{sc} and V_{oc} values the photocurrent–photovoltage (J–V) curves for the scrutinized dyes was generated, as depicted in Fig. 6. The J–V curve was derived using to the following equations:[77,78]

$$J = J_s \cdot \left(1 - e^{\frac{V}{K_B T}}\right) + J_{sc}$$

$$J_s = \frac{J_{sc}}{e^{\frac{qV_{oc}}{K_B T}} - 1}$$

where J_s represents the reverse saturation current. The fill factor (FF) of the dyes was also determined from Fig. 6. All the investigated dyes showcase excellent performance in terms of photoelectric conversion energy. **P-Pen-4-A2** and **P-Ant-4-A2** both featuring the same electron-attracting group, achieve impressive values of 29.72% and 27.90%, respectively, whereas **P-Pen-4-A1** and **P-Ant-4-A1** demonstrate slightly lower efficiency, with

Table 3 Calculated values of: reorganization energy λ (eV), electron injection distance, r_{inj} (Å), electron recombination distance, r_{rec} (Å), electron injection rate, k_{inj} (s^{-1}), electron recombination rate, k_{rec} (s^{-1}), electron collection efficiency, η_{coll}, electron injection efficiency, Φ_{inj}, short-circuit photocurrent density J_{sc} (mA cm^{-2}), open-circuit voltage V_{oc} (mV), fill factor FF and photoelectric conversion efficiency η (%)

Compound	λ	r_{inj}	r_{rec}	$k_{inj} \times 10^{12}$	$k_{rec} \times 10^{2}$	η_{coll}	Φ_{inj}	J_{sc}	V_{oc}	FF	η
P-Ant-4-A1@TiO_2	0.455	2.55	30.08	20.70	1.35	1	0.995	24.65	937	0.88	20.30
P-Ant-4-A2@TiO_2	0.446	2.53	37.12	2.81	0.03	1	0.967	28.15	1109	0.89	27.90
P-Pen-4-A1@TiO_2	0.482	2.89	29.74	40.48	8.16	1	0.998	32.29	884	0.88	25.01
P-Pen-4-A2@TiO_2	0.467	2.89	37.49	4.22	0.26	1	0.977	35.90	1012	0.82	29.72

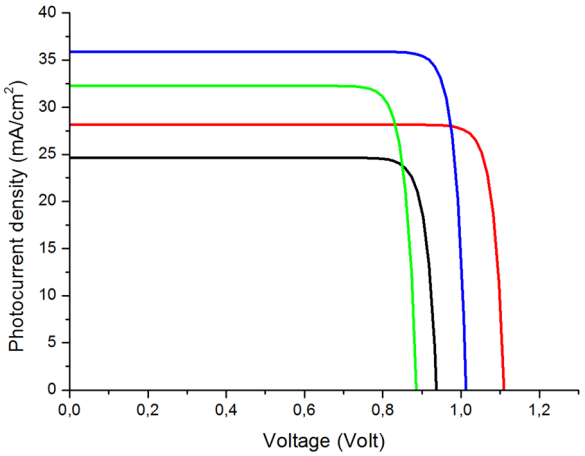

Fig. 6 Calculated J–V curves using the improved normal mode. Black line **P-Ant-4-A1** (V_{oc} = 0.937 V, J_{sc} = 24.65 mA, FF = 87.95%, η = 20.30); red line **P-Ant-4-A2** (V_{oc} = 1.109 V, J_{sc} = 28.15 mA, FF = 89.37%, η = 27.90); green line **P-Pen-4-A1** (V_{oc} = 0.884 V, J_{sc} = 32.29 mA, FF = 87.56%, η = 25.01); blue line **P-Pen-4-A2** (V_{oc} = 1.012 V, J_{sc} = 35.90 mA, FF = 81.79%, η = 29.72).

calculated η values of 25.01% and 20.30% respectively. By comparing with a reference such as the dye N719, utilized both in standalone and cosensitization applications, it is theoretically evident that the investigated dyes exhibit superior photovoltaic properties compared to the reference. Indeed, the performance of N719 reports a J_{sc} of 17.73 mA cm^{-2}, a V_{oc} value of 0.85 V, a PCE of 11.2%, and an absorption maximum wavelength at 538 nm.[79]

3.4 MD simulations

To evaluate the stability of the investigated structures, particularly with regard to the potential collapse onto the TiO_2 surface, targeted MD studies were conducted on structures featuring 4 conjugated triple bonds, namely **P-Ant-4-A1**, **P-Pen-4-A1**, **PAnt-4-A2** and **P-Pen-4-A2**. These structures inherently possess higher flexibility compared to those with only two conjugated triple bonds, making them more susceptible to reclining onto the surface. Throughout the simulation, fluctuations in three distinct distances, *d*1, *d*2 and *d*3, as depicted in Fig. 3 of the ESI,† were monitored. Graphs illustrating these fluctuations over time are shown in Fig. 7, revealing a notable rigidity of the analyzed structures, with minimal variations in all distances. Notably, *d*2 exhibits the most significant excursion, reflecting the flexibility conferred by the four conjugated triple bonds, yet it remains within the range of 11.5 to 12 Å. Furthermore, distances *d*2 and *d*3 remain near-constant values throughout the simulation. As a result, at a temperature of 298 K, there is no indication of collapse onto the surface.

4. Conclusions

We conducted a thorough DFT investigation into the spectroscopic and photoelectric properties of newly designed dyes that incorporate acene group in proximity to the donor moiety, specifically the 2-amino pyrrole. In our investigation, we considered two distinct withdrawing groups, the cyanoacrylate and a derivative of pyridinium salt group. Additionally, we

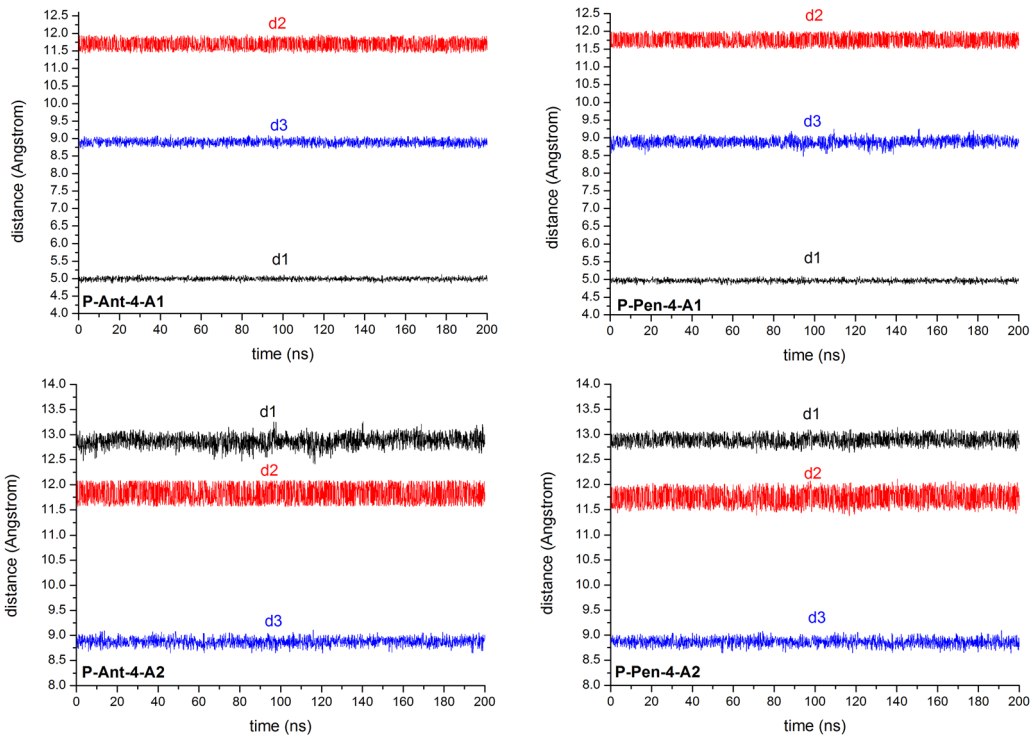

Fig. 7 Time fluctuation of distances *d*1, *d*2 and *d*3, see Fig. S3, ESI,† for **P-Ant-4-A1**, **P-Pen-4-A1**, **P-Ant-4-A2** and **P-Pen-4-A2** at 298 K.

employed linear carbon chains of varying lengths (LCCs) as π-bridge. The UV-vis spectra of these dyes showcase excellent absorption properties, with particular emphasis on the superior outcomes exhibited by dyes incorporating pentacene, whose absorption extends beyond 920 nm, significantly contributing to the observed panchromatic effect. Moreover, the investigation delves into the electron transfer process occurring at the interface between the dye and the semiconductor, emphasizing favorable interactions. The most promising results emerged with longer-chained polyynes, notably with the dyes **P-Ant-4-A2** and **P-Pen-4-A2** which revealed lower k_{rec} values, thereby resulting in highest V_{oc} values. Moreover, these dyes displayed superior J_{sc} values, highlighting the efficiency of the A2 group in comparison to cyanoacrylate. **P-Ant-4-A2** and **P-Pen-4-A2** demonstrated outstanding photoelectric conversion efficiency values of 27.90% and 29.72%. However, **P-Ant-4-A1** and **P-Pen-4-A1** exhibited significant PCE values of 20.30% and 25.01% respectively. Classical MD simulations reveal that, throughout the 200 ns simulation period, the dyes retain a vertically oriented adsorption configuration. These finding provide a robust foundation for synthesizing the designed dyes and their application, either as standalone sensitizers or in co-sensitizing configurations. The panchromatic characteristics of these metal free dyes, with absorption extending into the near IR region, hold promise for their application in photovoltaic technologies.

Author contributions

Giuseppe Consiglio: conceptualization, methodology, investigation, writing, revision and editing. Adam Gorcyński: investigation, writing, revision and editing. Guido Spoto: methodology, writing, revision and editing. Salvatore Petralia: investigation, writing, revision and editing. Giuseppe Forte: conceptualization, supervision, methodology, writing original draft.

Conflicts of interest

The authors declare no conflicts of interest.

Acknowledgements

This work has been partially funded by European Union (NextGeneration EU), through the MUR-PNRR project National Center for HPC, Big Data and Quantum Computing (E63C22001000006).

References

1 P. Y. Chen, J. Qi, M. T. Klug, X. Dang, P. T. Hammond and A. M. Belcher, *Energy Environ. Sci.*, 2014, **7**, 3659–3665.
2 B. O'Regan and M. Grätzel, *Nature*, 1991, **353**, 737–740.
3 F. Grifoni, M. Bonomo, W. Naim, N. Barbero, T. Alnasser, I. Dzeba, M. Giordano, A. Tsaturyan, M. Urbani, T. Torres, C. Barolo and F. Sauvage, *Adv. Energy Mater.*, 2021, **11**, 2101598.
4 Standard Tables for Reference Solar Spectral Irradiances: Direct Normal and Hemispherical on 37° Tilted Surface, 2023, **https://www.astm.org/g0173-23.html** (accessed: January 2024).
5 P. Brogdon, H. Cheema and J. H. Delcamp, *ChemSusChem*, 2018, **11**, 86–103.
6 M. Akhtaruzzaman, M. Shahiduzzaman, V. Selvanathan, K. Sopian, M. I. Hossain, N. Amin and A. K. Mahmud Hasa, *Appl. Mater. Today*, 2021, **25**, 101204.
7 M. K. Nazeeruddin, P. Péchy, T. Renouard, S. M. Zakeeruddin, R. Humphry-Baker, P. Comte, P. Liska, L. Cevey, E. Costa, V. Shklover, L. Spiccia, G. D. Deacon, C. A. Bignozzi and M. Grätzel, *J. Am. Chem. Soc.*, 2001, **123**, 1613–1624.
8 T. Swetha, P. J. S. Rana, A. Islam and S. P. Singh, *Sol. Energy*, 2019, **188**, 305–311.
9 E. J. Cho, J. K. Cha, G. Fu, H. S. Cho, H. W. Lee and S. H. Kim, *J. Ind. Eng. Chem.*, 2022, **115**, 272–278.
10 G. Fu, E. J. Cho, X. Luo, J. Cha, J. H. Kim, H. W. Lee and S. H. Kim, *Sol. Energy*, 2021, **218**, 346–353.
11 M. R. E. da Silva, T. Auvray and G. S. Hanan, *Inorg. Chim. Acta*, 2020, **499**, 119194.
12 J. D. Cheng, C. X. He, D. Chen, X. Y. Gu, S. K. Wang, X. P. Gao, G. Z. Sun, Z. X. Zhang, X. J. Pan, X. B. Pan and J. Y. Zhou, *Opt. Mater.*, 2022, **133**, 112924.
13 C. Y. Chen, Y. M. Feng, T. Y. Wu, Y. C. Liu, S. Y. Chen, T. Y. Lin, H. H. G. Tsai and C. G. Wu, *Appl. Energy Mater.*, 2021, **4**, 13461–13470.
14 W. Sharmoukh, W. M. I. Hassan, P. C. Gros and N. K. Allam, *RSC Adv.*, 2016, **6**, 69647–69657.
15 B. A. Ali, W. Sharmoukh, M. M. Elnagar, Z. M. Hassan and N. K. Allam, *Appl. Organomet. Chem.*, 2019, **33**, e4677.
16 A. Yella, H. W. Lee, H. N. Tsao, C. Yi, A. K. Chandiran, M. K. Nazeeruddin, E. W. G. Diau, C. Y. Yeh, S. M. Zakeeruddin and M. Grätzel, *Science*, 2011, **334**, 629–634.
17 S. Mathew, A. Yella, P. Gao, R. Humphry-Baker, B. F. Curchod, N. Ashari-Astani, I. Tavernelli, U. Rothlisberger, M. K. Nazeeruddin and M. Grätzel, *Nat. Chem.*, 2014, **6**, 242–247.
18 G. Consiglio, S. Failla, C. G. Fortuna, L. D'Urso and G. Forte, *Comput. Theor. Chem.*, 2015, **1067**, 1–6.
19 I. P. Oliveri, G. Forte, G. Consiglio, S. Failla and S. Di Bella, *Inorg. Chem.*, 2017, **56**, 14206–14213.
20 S. Aghazada, P. Gao, A. Yella, G. Marotta, T. Moehl, J. Teuscher, J. E. Moser, F. De Angelis, M. Grätzel and M. K. Nazeeruddin, *Inorg. Chem.*, 2016, **55**, 6653–6659.
21 N. V. Krishna, J. V. S. Krishna, M. Mrinalini, S. Prasanthkumar and L. Giribabu, *ChemSusChem*, 2017, **10**, 4668–4689.
22 C. C. Chen, J. S. Chen, V. S. Nguyen, T. C. Wei and C. Y. Yeh, *Angew. Chem.*, 2021, **60**(9), 4886–4893.
23 G. Di Carlo, A. Orbelli Biroli, F. Tessore, M. Pizzotti, P. R. Mussini, A. Amat, F. De Angelis, A. Abbotto,

V. Trifiletti and R. Ruffo, *J. Phys. Chem. C*, 2014, **118**, 7307–7320.
24 J. Luo, Z. Xie, J. Zou, X. Wu, X. Gong, C. Li and Y. Xie, *Chin. Chem. Lett.*, 2022, **33**, 4313–4316.
25 Y. Chen, Y. Tang, J. Zou, K. Zeng, G. Baryshnikov, C. Li and Y. Xie, *ACS Appl. Mater. Interfaces*, 2021, **13**, 49828–49839.
26 K. Zeng, Y. Chen, W. H. Zhu, H. Tian and Y. Xie, *J. Am. Chem. Soc.*, 2020, **142**, 5154–5161.
27 J. Zou, Y. Wang, G. Baryshnikov, J. Luo, X. Wang, H. Ågren, C. Li and Y. Xie, *ACS Appl. Mater. Interfaces*, 2022, **14**, 33274–33284.
28 S. Erten-Ela, Y. Ueno, T. Asaba and Y. Kubo, *New J. Chem.*, 2017, **41**, 10367–10375.
29 V. Punitharasu, M. F. M. Kavungathodi, A. K. Singh and J. Nithyanandhan, *Appl. Energy Mater.*, 2019, **2**, 8464–8472.
30 A. Islam, T. H. Chowdhury, C. Quin, L. Han, J. J. Lee, I. M. Bedja, M. Akhtaruzzaman, K. Sopian, A. Mirloup and N. Leclerc, *Sustainable Energy Fuels*, 2018, **2**, 209–214.
31 M. Golshan, S. Osfouri, R. Azin, T. Jalali and N. R. Moheimani, *J. Photochem. Photobiol., A*, 2021, **417**, 113345.
32 A. K. Singh and J. Nithyanandhan, *Appl. Energy Mater.*, 2022, **5**, 1858–1868.
33 R. Haridas, N. Ajikumar, J. Velore, N. A. Philip, C. H. Suresh, S. Soman and K. Yoosaf, *ChemistrySelect*, 2023, **8**, e202303508.
34 G. Consiglio, A. Gorcynski, S. Petralia and G. Forte, *RSC Adv.*, 2023, **13**, 1019–1030.
35 G. Consiglio, A. Gorcynski, S. Petralia and G. Forte, *Dalton Trans.*, 2023, **52**, 15995–16004.
36 G. Consiglio, A. Gorcynski, S. Petralia and G. Forte, *J. Mater. Chem. C*, 2024, **12**, 903–912.
37 C. Y. Lin, Y. C. Wang, S. J. Hsu, C. F. Lo and E. W. Diau, *J. Phys. Chem. C*, 2010, **114**, 687–693.
38 W. Li, J. Wang, J. Chen, F. Q. Bai and H. X. Zhang, *Phys. Chem. Chem. Phys.*, 2014, **16**, 9458–9468.
39 W. Li, F. Q. Bai, J. Chen, J. Wang and H. X. Zhang, *J. Power Sources*, 2015, **275**, 207–216.
40 G. Forte, L. D'Urso, E. Fazio, S. Patanè, F. Neri, O. Puglisi and G. Compagnini, *Appl. Surf. Sci.*, 2013, **272**, 76–81.
41 E. Fazio, L. D'Urso, G. Consiglio, A. Giuffrida, G. Compagnini, O. Puglisi, S. Patanè, F. Neri and G. Forte, *J. Phys. Chem. C*, 2014, **118**, 28812–28819.
42 C. S. Casari, M. Tommasini, R. R. Tykwinski and A. Milani, *Nanoscale*, 2016, **8**, 4414–4435.
43 N. R. Agarwai, A. Lucotti, M. Tommasini, W. A. Chalifoux and R. R. Tykwinski, *J. Phys. Chem. C*, 2016, **120**(20), 11131–11139.
44 L. K. Zaitriand and S. M. Mekelleche, *Mol. Phys.*, 2020, **118**, 1–10.
45 P. Marabotti, A. Milani, A. Lucotti, L. Brambilla, M. Tommasini, C. Castiglioni, P. Mecik, B. Pigulski, S. Szafert and C. S. Casari, *Carbon Trends*, 2021, **5**, 100115.
46 P. Tomasella, V. Sanfilippo, C. Bonaccorso, L. M. Cucci, G. Consiglio, A. Nicosia, P. G. Mineo, G. Forte and C. Satriano, *Appl. Sci.*, 2020, **10**, 5529.
47 W. H. Liu, I. C. Wu, C. H. Lai, C.-H. Lai, P. T. Chou, Y. T. Li, C. L. Chen, Y. Y. Hsu and Y. Chi, *Chem. Commun.*, 2008, 5152–5154.
48 Y. Gao, X. Li, Y. Hu, Y. Fan, J. Yuan, N. Robertson and S. R. Marder, *J. Mater. Chem. A*, 2016, **4**, 12865–12877.
49 K. Wagner, P. Wagner, F. Hasani, J. E. Barnsley, K. C. Gordon, A. Lennert, D. M. Guldi and D. L. Officer, *Dyes Pigm.*, 2021, **186**, 109002.
50 M. J. Frisch, G. W. Trucks, H. B. Schlegel, G. E. Scuseria, M. A. Robb, J. R. Cheeseman, G. Scalmani, V. Barone, G. A. Petersson, H. Nakatsuji, X. Li, M. Caricato, A. V. Marenich, J. Bloino, B. G. Janesko, R. Gomperts, B. Mennucci, H. P. Hratchian, J. V. Ortiz, A. F. Izmaylov, J. L. Sonnenberg, D. Williams-Young, F. Ding, F. Lipparini, F. Egidi, J. Goings, B. Peng, A. Petrone, T. Henderson, D. Ranasinghe, V. G. Zakrzewski, J. Gao, N. Rega, G. Zheng, W. Liang, M. Hada, M. Ehara, K. Toyota, R. Fukuda, J. Hasegawa, M. Ishida, T. Nakajima, Y. Honda, O. Kitao, H. Nakai, T. Vreven, K. Throssell, J. A. Montgomery, Jr., J. E. Peralta, F. Ogliaro, M. J. Bearpark, J. J. Heyd, E. N. Brothers, K. N. Kudin, V. N. Staroverov, T. A. Keith, R. Kobayashi, J. Normand, K. Raghavachari, A. P. Rendell, J. C. Burant, S. S. Iyengar, J. Tomasi, M. Cossi, J. M. Millam, M. Klene, C. Adamo, R. Cammi, J. W. Ochterski, R. L. Martin, K. Morokuma, O. Farkas, J. B. Foresman and D. J. Fox, *Gaussian 16 Rev C.01*, Gaussian, Inc., Wallingford CT, 2016.
51 J. Preat, C. Michaux, D. Jacquemin and E. A. Perpete, *J. Phys. Chem. C*, 2009, **113**, 16821–16833.
52 M. Pastore, E. Mosconi, F. De Angelis and M. Gratzel, *J. Phys. Chem. C*, 2010, **114**, 7205–7212.
53 D. Fadili, Z. M. E. Fahim, S. M. Bouzzine, O. T. Alaoui and M. Hamidi, *Comput. Theor. Chem.*, 2022, **1210**, 113645.
54 C. O'Rourke and D. Bowler, *J. Phys.: Condens. Matter*, 2014, **26**, 195302.
55 M. Wagstaffe, A. G. Thomson, M. J. Jackman, M. Torres-Molina, K. L. Syres and K. Handrup, *J. Phys. Chem. C*, 2016, **120**(3), 1693–1700.
56 P. Giannozzi, O. Andreussi, T. Brumme, O. Bunau, M. Buongiorno Nardelli, M. Calandra, R. Car, C. Cavazzoni, D. Ceresoli, M. Cococcioni, N. Colonna, I. Carnimeo, A. Dal Corso, S. de Gironcoli, P. Delugas, R. A. DiStasio Jr, A. Ferretti, A. Floris, G. Fratesi, G. Fugallo, R. Gebauer, U. Gerstmann, F. Giustino, T. Gorni, J. Jia, M. Kawamura, H.-Y. Ko, A. Kokalj, E. Küçükbenli, M. Lazzeri, M. Marsili, N. Marzari, F. Mauri, N. L. Nguyen, H.-V. Nguyen, A. Otero-de-la-Roza, L. Paulatto, S. Poncé, D. Rocca, R. Sabatini, B. Santra, M. Schlipf, A. P. Seitsonen, A. Smogunov, I. Timrov, T. Thonhauser, P. Umari, N. Vast, X. Wu and S. Baroni, *J. Phys.: Condens. Matter*, 2017, **29**, 465901.
57 P. Giannozzi, O. Baseggio, P. Bonfà, D. Brunato, R. Car, I. Carnimeo, C. Cavazzoni, S. de Gironcoli, P. Delugas, F. Ferrari Ruffino, A. Ferretti, N. Marzari, I. Timrov, A. Urru and S. Baroni, *J. Chem. Phys.*, 2020, **152**, 154105.
58 M. J. Abraham, T. Murtola, R. Schulz, S. Pall, J. C. Smith, B. Hess and E. Lindahal, *Software X*, 2015, **1**, 19–25.

59 W. L. Jorgensen, D. S. Maxwell and J. Tirado-Rives, *J. Am. Chem. Soc.*, 1996, **118**, 11225–11236.
60 T. Morishita, *J. Chem. Phys.*, 2000, **113**, 2976–2982.
61 M. Di Pierro, R. Elber and B. Leimkuhler, *J. Chem. Theory Comput.*, 2015, **11**, 5624–5637.
62 C. Satriano, M. E. Fragalà, G. Forte, A. M. Santoro, D. La Mendola and B. Kasemo, *Soft Matter*, 2012, **8**, 53–56.
63 M. Grätzel, *Acc. Chem. Res.*, 2009, **42**, 1788–1798.
64 J. W. Ondersma and T. W. Hamann, *Coord. Chem. Rev.*, 2013, **257**, 1533–1543.
65 A. Yella, H. W. Lee, H. N. Tsao, C. Yi, A. K. Chandiran, M. K. Nazeeruddin, E. W. G. Diau, C. Y. Yeh, S. M. Zakeeruddin and M. Grätzel, *Science*, 2011, **334**, 629–634.
66 S. Haid, M. Marszalek, A. Mishra, M. Wielopolski, J. Teuscher, J. E. Moser, R. Humphry-Baker, S. M. Zakeeruddin, M. Grätzel and P. Baurle, *Adv. Funct. Mater.*, 2012, **22**, 1291–1302.
67 N. Vlachopoulos, P. Liska, J. Augustynski and M. Grätzel, *J. Am. Chem. Soc.*, 1988, **110**, 1216–1220.
68 T. J. Meade, H. B. Gray and J. R. Winkler, *J. Am. Chem. Soc.*, 1989, **111**, 4353–4356.
69 M. P. Balany and D. H. Kim, *THEOCHEM*, 2009, **910**, 20–26.
70 S. R. Raga, E. M. Barea and F. Fabregat-Santiago, *J. Phys. Chem. Lett.*, 2012, **3**, 1629–1634.
71 D. P. Hagberg, T. Marinado, K. M. Karlsson, K. Nonomura, P. Quin, G. Boschloo, T. Brinck, A. Hagfeldt and L. Sun, *J. Org. Chem.*, 2007, **72**, 9550–9556.
72 S. Mohakud and S. K. Pati, *J. Mater. Chem.*, 2009, **19**, 4356–4361.
73 A. Datta, S. Mohakud and S. K. Pati, *J. Chem. Phys.*, 2007, **126**, 144710–144717.
74 J. Preat, A. Hagfeldt and E. A. Perpete, *Energy Environ. Sci.*, 2011, **4**, 4537–4549.
75 J. B. Asbury, Y. Q. Wang, E. C. Hao, H. N. Ghosh and T. Q. Lian, *Res. Chem. Intermed.*, 2001, **27**, 393–406.
76 H. W. Ham and Y. S. Kim, *Thin Solid Films*, 2010, **518**, 6558–6563.
77 K. Srinivas, K. Yesudas, K. Bhanuprakash, V. J. Rao and L. Giribabu, *J. Phys. Chem. C*, 2009, **113**, 20117–20126.
78 L. Sicot, B. Geffroy, A. Lorin, P. Raimond, C. Sentein and J. M. Nunzi, *J. Appl. Phys.*, 2001, **90**, 1047–1054.
79 R. Buscaino, C. Baiocchi, C. Barolo, C. Medana, M. Grätzel and M. K. Nazeeruddin, *Inorg. Chim. Acta*, 2008, **362**, 798–805.